


## RESEARCH ARTICLE

# Parameterizing building effects on airflows within the urban canopy layer for high-resolution models using a nudging approach

Ge Cheng<sup>1</sup>  | K. Heinke Schlünzen<sup>1</sup> | David Grawe<sup>2</sup> | Vivien Voss<sup>1</sup> | Marcus Thatcher<sup>3</sup> | Peter Rayner<sup>4</sup>

<sup>1</sup>Meteorological Institute, Center for Earth System Research and Sustainability (CEN), Universität Hamburg, Hamburg, Germany

<sup>2</sup>Center for Earth System Research and Sustainability (CEN), Meteorological Institute, Universität Hamburg, Hamburg, Germany

<sup>3</sup>Oceans and Atmosphere, CSIRO, Aspendale, Victoria Australia

<sup>4</sup>School of Earth Sciences, Climate and Energy College, University of Melbourne, Parkville, Victoria, Australia

## Correspondence

Ge Cheng, Meteorological Institute, Center for Earth System Research and Sustainability (CEN), Universität Hamburg, Hamburg 20146, Germany.  
Email: [ge.cheng@uni-hamburg.de](mailto:ge.cheng@uni-hamburg.de)

## Funding information

Deutsche Forschungsgemeinschaft (DFG, German Research Foundation) under Germany's Excellence Strategy-EXC 2037 'CLICCS-Climate, Climatic Change, and Society', Grant/Award Number: 390683824

## Abstract

In this study, a new multilayer urban canopy parameterization for high-resolution (~1 km) atmospheric models using the nudging approach to represent the impacts of urban canopies on airflow is presented. In our parameterization, a nudging term is added to the momentum equations and a source term to the turbulent kinetic energy equation to account for building effects. The challenge of this parameterization lies in defining appropriate values for the nudging coefficient and the weighting function used to reflect canopy effects. Values of both are derived and the parameterization developed is implemented and tested for idealized cases in the Mesoscale Transport and Stream model (METRAS). Comparison data are taken from obstacle-resolving microscale model results. Results show that the parameterization using the nudging approach can simulate aerodynamic effects induced within the canopy by obstacles well, in terms of reduction of wind speeds and production of additional turbulent kinetic energy. Thus, models with existing nudging can use this approach as an efficient and effective method to parameterize dynamic urban canopy effects.

## KEYWORDS

canopy parameterization, evaluation, nudging, numerical modelling, urban boundary layer, urban canopy parameterization

## 1 | INTRODUCTION

Information about flow characteristics within and above urban canopies is required in various urban studies, including urban air pollution modelling, urban wind energy, urban planning, building design, and so forth. The

impacts of urban canopies on local climate include drag induced by buildings with consequent loss of momentum, enhancement of the conversion of mean kinetic energy into turbulence kinetic energy, and modification of heat fluxes due to shadowing and radiation-trapping effects (Roth, 2000; Martilli *et al.*, 2002; Garuma, 2018;

Cheng and Schlünzen, 2023). These impacts may be different at different vertical levels in the canopy. For instance, due to the presence of obstacles, shadowing effects within canopies are enhanced and more short-wave radiation is reflected within canopies than above canopies. In contrast, the aerodynamic effects of urban canopies might be similar at different heights: for example, the reduction in wind speed and turbulence intensity occurs at ground level and within canopies (Cheng and Schlünzen, 2023). However, the intensity depends on the density of the buildings and their height.

To reproduce the aerodynamic effects of urban canopies in high-resolution (~1 km resolution) atmospheric models, two approaches are commonly used. The first approach is the roughness approach, which uses a gridded roughness length and a displacement height to represent the impacts of surface obstacles on the mean airflow. The roughness-length approach is based on Monin–Obukhov similarity theory, which assumes stationary conditions and horizontal homogeneity. This approach is only implemented for the lowest atmospheric model layer. The second approach is the drag-force approach (Brown, 2000; Dupont *et al.*, 2004). In this approach, a term is added to the momentum and turbulence kinetic energy (TKE) equations of atmospheric models to account for obstacle drag. The approach allows representation of urban canopy effects down to the surface and up to the height of the highest obstacle (Masson, 2006).

Both the roughness-length and drag-force approaches have advantages: for instance, the roughness-length approach is easy to implement and is generally used in atmospheric models, while the drag-force approach can capture the flow dynamics within canopies and the drag term considers the height dependence of the obstacles' density. However, the different approaches also have drawbacks. The main drawback of the roughness-length approach is that it assumes a horizontal surface homogeneity within the roughness sublayer using the constant-flux layer theory, and this simplicity sacrifices the realistic representation of atmospheric phenomena in urban canopies. The roughness approach can be satisfactory for modelling overall urban impacts on the atmosphere, but is not sufficient for generating more detailed meteorological fields, such as reproducing maximum observed TKE at the top of the urban canopy or reproducing the roughness sublayer over urban surfaces (Martilli *et al.*, 2002; Otte *et al.*, 2004; Garuma, 2018). The main disadvantage of the drag-force approach is that there is difficulty in determining the values of the drag coefficient, especially for urban areas with highly complex surface geometries (Brown, 2000; Masson, 2000). In addition, this approach requires more computational time

and more detailed information about urban morphology (Grimmond *et al.*, 2009).

To overcome the drawbacks of the roughness-length and drag-force approaches, a novel approach based on the nudging concept is developed in this study. The adjusted nudging approach is designed to simply and efficiently represent the aerodynamic effects of urban surfaces on airflow at multiple levels within and above canopies and accounts for horizontal surface heterogeneity within the roughness sublayer. Nudging or Newtonian relaxation is a common method used in downscaling and data assimilation that adjusts the model dynamically towards forcing data, frequently towards observations. The basic idea of nudging is to insert a nonphysical linear diffusion term (the nudging term) that is proportional to the model – observation difference in the governing model equations so that the model is “nudged” towards the observations (Hoke and Anthes, 1976). Numerous studies have been presented describing the benefits of using nudging to constrain the evolution of a numerical model, but no studies have explored the ability of nudging to be served as a canopy parameterization.

The main advantage of using nudging as an urban canopy parameterization is that this approach is easy to implement and there is low computational demand. Besides this, nudging as a downscaling and data assimilation approach has already been implemented in many mesoscale models: for example, the Consortium for Small-scale Modeling (COSMO: Bollmeyer *et al.*, 2015; Schraff *et al.*, 2016), Mesoscale Transport and Stream model (METRAS: Dierer *et al.*, 2005a; Dierer and Schlünzen, 2005b; Ries *et al.*, 2010), Fifth-Generation Penn State/NCAR Mesoscale Model (MM5: Nielsen-Gammon *et al.*, 2007; Vinodkumar *et al.*, 2008; Choi *et al.*, 2009; Park *et al.*, 2011; Solman and Pessacg, 2012), and Weather Research and Forecasting (WRF: Srinivas *et al.*, 2010; Liu *et al.*, 2013; Bullock *et al.*, 2014; Wang *et al.*, 2018), as well as global models: for example, the Community Atmosphere Model version 6 (CAM6: Kruse *et al.*, 2022), ECHAM (Bauer and Wulfmeyer, 2009), and Icosahedral Nonhydrostatic Weather and Climate Model (ICON: Zängl *et al.*, 2022). This means that no additional effort is required to develop the approach itself; efforts are only required to determine the value of the nudging term, with which canopy effects are represented in models.

The article is organized as follows: Section 2 describes the nudging approach and the numerical model used. In Section 2.3 the new canopy parameterization based on the nudging approach is introduced. Section 3 describes the model setup for the test simulations, the comparison datasets for evaluation, and the parameter adjustment. In Section 4, simulation results of METRAS are compared with an obstacle-resolving microscale model dataset, in

particular with respect to mean wind speeds and turbulence kinetic energy. Finally, conclusions are drawn in Section 5.

## 2 | METHODS

### 2.1 | Nudging

Let  $\psi(\mathbf{x}, t)$  be a prognostic variable to be nudged. Nudging introduces an artificial tendency term, the so-called nudging term, into the tendency equations for the prognostic variable. The general form for the predictive equation of variable  $\psi(\mathbf{x}, t)$  being nudged is written as follows:

$$\frac{\partial}{\partial t} \psi(\mathbf{x}, t) = F(\psi, \mathbf{x}, t) - \underbrace{\mathcal{W}(\mathbf{x}) \cdot \delta \cdot [\psi(\mathbf{x}, t) - \psi^F(\mathbf{x}, t)]}_{\text{Nudging term}}, \quad (1)$$

where  $\psi(\mathbf{x}, t)$  is the predicted value computed by the model,  $\mathbf{x}$  is the time-independent spatial variable,  $t$  is the time,  $F(\psi, \mathbf{x}, t)$  denotes the model's physical forcing terms (e.g. pressure gradient force, Coriolis force, advection, etc.),  $\mathcal{W}(\mathbf{x})$  is the weighting function (nondimensional),  $\delta$  is the nudging coefficient ( $\text{s}^{-1}$ ), and  $\psi^F(\mathbf{x}, t)$  is the forcing data. The second term on the right side of the equation denotes the nudging term, proportional to the difference between the model state and the forcing data.

The nudging term is a nonphysical linear diffusion term. Zou *et al.* (1992) mentioned that the nudging term should be large enough to impact simulations, but still be small enough that it will not completely dominate the time tendency in the governing equation. According to Stensrud and Bao (1992), the nudging term is roughly an order of magnitude smaller than the other terms in the governing equation. Bollmeyer *et al.* (2015) stated that the nudging term remains smaller than the largest term of the original model forcing.

Simulation results are highly dependent on the product of nudging coefficient  $\delta$  and weighting function  $\mathcal{W}(\mathbf{x})$ . If the model physical forcing terms  $F(\psi, \mathbf{x}, t)$  are neglected and a weighting function  $\mathcal{W}(\mathbf{x})$  equal to 1 is assumed, then the prognostic variable state  $\psi(\mathbf{x}, t)$  relaxes exponentially towards the forcing data  $\psi^F(\mathbf{x}, t)$  with an  $e$ -folding decay rate of  $1/\delta$ . The decay rate describes how much time the model needs until  $\psi(\mathbf{x}, t)$  is adjusted by a factor of  $e$  to  $\psi^F(\mathbf{x}, t)$ . Relatively small values of  $\delta$  induce more gradual modification, which helps limit dynamic imbalances that could cause an unstable solution. As the numerical stability criterion must be satisfied,  $\delta$  should follow  $\delta \Delta t \leq 1$ , where  $\Delta t$  is the time step (Stauffer *et al.*, 1991). Previous studies showed that typical values of  $\delta$  are  $10^{-4}$  to  $10^{-3} \text{ s}^{-1}$  for meteorological systems (Stauffer *et al.*, 1991;

Choi *et al.*, 2009; Korsholm *et al.*, 2015). For example, the default value for the nudging coefficient in MM5 and WRF models is set to  $3 \times 10^{-4} \text{ s}^{-1}$ . The values vary depending on the nudged variables, that is, wind component, temperature, surface pressure, vorticity, and so forth.

The weighting function  $\mathcal{W}(\mathbf{x})$  has a value between 0 and 1. Often nudging is only performed at the model boundaries; however, the data (e.g., measurements) might also be distributed unevenly in space (Koopmans *et al.*, 2023).  $\mathcal{W}(\mathbf{x})$  can be a spatial function, usually with a maximum amplitude of unity where the distance between the forcing data and nudging grid point is smallest, decreasing to zero at other grid points (Brill *et al.*, 1991). For nesting, the values of  $\mathcal{W}(\mathbf{x})$  may be larger at the lateral boundaries than in the inner of the model domain (Källberg, 1977; Ries *et al.*, 2010), and for initialization they may be higher, reducing in time (Dierer *et al.*, 2005a). Moreover, the value of  $\mathcal{W}(\mathbf{x})$  can also depend on the time, quality, and character as well as accuracy of the forcing data (Hoke and Anthes, 1976; Brill *et al.*, 1991; Stauffer *et al.*, 1991).

The forcing data  $\psi^F(\mathbf{x}, t)$  are external data sources that are used to drive the numerical model. The forcing data variables are consistent with the nudged variables, such as wind component, temperature, pressure, humidity, precipitation, concentrations, soil moisture, velocity divergence, vorticity, and so forth. Depending on various applications, nudging has been developed to include different types of synoptic data as forcing data in numerical weather prediction systems, such as in situ observations (Choi *et al.*, 2009), radiosondes, radar, wind profiler, satellite, and aircraft measurements (Schraff, 1997; Nielsen-Gammon *et al.*, 2007; Vinodkumar *et al.*, 2008; Srinivas *et al.*, 2010; Liu *et al.*, 2013), model results (Dierer *et al.*, 2005a), or reanalysis data (Dierer *et al.*, 2005a; Bauer and Wulfmeyer, 2009; Ries *et al.*, 2010; Park *et al.*, 2011; Peings *et al.*, 2012).

Nudging is commonly used in operational numerical weather prediction because of its easy implementation and low computational demands; however, the method has its disadvantages. First, there is difficulty in determining the nudging coefficient and weighting function. Usually, they are adjusted empirically in sensitivity experiments and cannot be determined by using a theoretically optimal solution to the analysis problem through a mathematic formalism (Bollmeyer *et al.*, 2015). Secondly, correlations between observation and model errors are not employed explicitly for this approach (Bauer and Wulfmeyer, 2009). Thirdly, nudging does not conserve energy. As a nonphysical linear diffusion term is added to the governing equation, energy is lost at each time step due to nudging. Keeping the difficulties in mind, nudging may be employed for parameterizing building effects (Section 2.3).

## 2.2 | METRAS model description

For the present study, nudging is extended to become the new canopy parameterization (Section 2.3) implemented in the METRAS model (Schlünzen, 1990). METRAS is a three-dimensional, nonhydrostatic model on surface fitted grids based on the conservation equations for momentum, mass, and energy, simplified by using the Boussinesq approximation, anelastic assumption, and may use a domain-constant Coriolis parameter for a small model domain (Schlünzen *et al.*, 2018). METRAS solves the prognostic equations for horizontal and vertical wind components, temperature, specific humidity, cloud water, rain-water content, and concentrations in flux form; density and pressure are derived from diagnostic equations. The model state variables are staggered using an Arakawa C-grid (Arakawa and Lamb, 1977). Subgrid-scale land-use representation and surface subgrid-scale characteristics are considered in the model via flux aggregation (von Salzen *et al.*, 1996; Schlünzen and Katzfey, 2003). Urban influences are considered using a slab model (roughness approach) that shows similar results to the Building Effect Parameterization (BEP) which is a complex canopy parameterization (Grawe *et al.*, 2013b).

The subgrid-scale turbulent fluxes are parameterized by a first-order closure which employs exchange coefficients. The exchange coefficient below  $z = 10$  m (the lowest layer in METRAS) is calculated based on Monin–Obukhov surface-layer similarity theory with the near-surface turbulent fluxes calculated by the flux-averaging method using the concept of blending height (von Salzen *et al.*, 1996). To determine the exchange coefficient above  $z = 10$  m, a Prandtl–Kolmogorov closure is used in the present applications, which uses a mixing length and solves a prognostic equation for the subgrid-scale turbulence kinetic energy.

As mentioned in Section 2.1, there are no specific criteria on determining the value of nudging coefficient  $\delta$ ; the proper values are usually found empirically through sensitivity tests. For a standard nudging in METRAS to observations with a resolution of 1–5 km,  $\delta$  is set to  $10^{-3} \text{ s}^{-1}$  (Davies, 1976; Källberg, 1977), which is equivalent to a forcing time-scale of approximately 30 min at the boundaries. For an intensified nudging during initialization, the value is increased to  $10^{-2} \text{ s}^{-1}$  (Ries *et al.*, 2010), resulting in a characteristic time of about 2 min at the boundaries. For nesting METRAS into ECMWF reanalyses data, a decrease of  $\mathcal{W}(\mathbf{x})$  from one at the open boundaries to zero in the inner part of the model domain is implemented, so that METRAS results are consistent with reanalysis data at the boundaries (Ries *et al.*, 2010).

## 2.3 | Canopy parameterization by using the nudging approach

In the current study, we focus on parameterizing aerodynamic effects, that is, representing the reduction of mean wind speeds and production of TKE due to the presence of obstacles in urban areas. We assume that there are no winds within buildings, which reflects the reality, and set the forcing field  $\psi^F(\mathbf{x}, t)$  in Equation 1 to zero. Note that this is different from obstacle-resolving models, which typically use a building-mask concept and set the prognostic variable  $\psi(\mathbf{x}, t)$  of the building-covered grid cells directly to zero (Salim *et al.*, 2018). Equation 1 is rewritten for horizontal wind fields  $U(\mathbf{x}, t)$  as follows:

$$\frac{\partial}{\partial t} U(\mathbf{x}, t) = F(U, \mathbf{x}, t) - \underbrace{\mathcal{W}(\mathbf{x}) \cdot \delta \cdot U(\mathbf{x}, t)}_{\text{Nudging term}} \quad (2)$$

METRAS is based on the Reynolds-averaged Navier–Stokes equations for describing the flow evolution. Employing Equation 2, the prognostic equations of horizontal wind components  $\bar{u}$  and  $\bar{v}$  are calculated as follows in flux form (Schlünzen *et al.*, 2018), neglecting the coordinate transformation for simplicity:

$$\begin{aligned} \frac{\partial \rho_0 \alpha^* \bar{u}}{\partial t} = & \underbrace{-\frac{\partial}{\partial x} (\bar{u} \rho_0 \alpha^* \bar{u}) - \frac{\partial}{\partial y} (\bar{v} \rho_0 \alpha^* \bar{u}) - \frac{\partial}{\partial z} (\bar{w} \rho_0 \alpha^* \bar{u})}_{\text{Advection}} \\ & \underbrace{-\alpha^* \left( \frac{\partial \bar{p}}{\partial x} \right)}_{\text{Pressure-gradient force}} + \underbrace{+ f \rho_0 \alpha^* (\bar{v} - V_g) - f' \rho_0 \alpha^* \bar{w}}_{\text{Coriolis force}} \\ & \underbrace{+ \frac{\partial}{\partial x} \left( 2 \rho_0 \alpha^* K_{hm} \frac{\partial \bar{u}}{\partial x} \right) + \frac{\partial}{\partial y} \left[ \rho_0 \alpha^* K_{hm} \left( \frac{\partial \bar{u}}{\partial y} + \frac{\partial \bar{v}}{\partial x} \right) \right]}_{\text{Force by turbulent fluxes}} \\ & \underbrace{+ \frac{\partial}{\partial z} \left[ \rho_0 \alpha^* K_{vm} \left( \frac{\partial \bar{u}}{\partial z} + \frac{\partial \bar{w}}{\partial x} \right) \right]}_{\text{Force by turbulent fluxes}} \\ & \underbrace{- \mathcal{W}(x, y, z) \delta \rho_0 \alpha^* \bar{u}}_{\text{Nudging term}} \end{aligned} \quad (3a)$$

$$\begin{aligned} \frac{\partial \rho_0 \alpha^* \bar{v}}{\partial t} = & \underbrace{-\frac{\partial}{\partial x} (\bar{u} \rho_0 \alpha^* \bar{v}) - \frac{\partial}{\partial y} (\bar{v} \rho_0 \alpha^* \bar{v}) - \frac{\partial}{\partial z} (\bar{w} \rho_0 \alpha^* \bar{v})}_{\text{Advection}} \\ & \underbrace{-\alpha^* \left( \frac{\partial \bar{p}}{\partial y} \right)}_{\text{Pressure-gradient force}} + \underbrace{- f \rho_0 \alpha^* (\bar{u} - U_g)}_{\text{Coriolis force}} \\ & \underbrace{+ \frac{\partial}{\partial x} \left[ \rho_0 \alpha^* K_{hm} \left( \frac{\partial \bar{u}}{\partial y} + \frac{\partial \bar{v}}{\partial x} \right) \right] + \frac{\partial}{\partial y} \left( 2 \rho_0 \alpha^* K_{hm} \frac{\partial \bar{v}}{\partial y} \right)}_{\text{Force by turbulent fluxes}} \\ & \underbrace{+ \frac{\partial}{\partial z} \left[ \rho_0 \alpha^* K_{vm} \left( \frac{\partial \bar{v}}{\partial z} + \frac{\partial \bar{w}}{\partial y} \right) \right]}_{\text{Force by turbulent fluxes}} \\ & \underbrace{- \mathcal{W}(x, y, z) \delta \rho_0 \alpha^* \bar{v}}_{\text{Nudging term}} \end{aligned} \quad (3b)$$

Here  $\bar{u}$ ,  $\bar{v}$ , and  $\bar{w}$  are the Reynolds-averaged wind-velocity components in the Cartesian coordinates,  $\rho_0$  is the

basic-state part of the density,  $\alpha^*$  is the grid volume,  $\tilde{p}$  is the pressure deviation, and  $U_g$  and  $V_g$  are the horizontal components of geostrophic wind, which result from the balance between the Coriolis force and the large-scale pressure gradient. The Coriolis parameters  $f = 2\Omega \sin \varphi$  and  $f' = 2\Omega \cos \varphi$  are calculated according to the local geographic latitude  $\varphi$  and the angular velocity of the Earth's rotation  $\Omega$ .  $K_{hm}$  and  $K_{vm}$  denote the horizontal and vertical exchange coefficient, respectively. The last term on the right side of the equation is the nudging term, with a negative sign representing the momentum sink.

In this study,  $\delta$  in the nudging term is set to  $5 \times 10^{-3} \text{ s}^{-1}$ , which is determined empirically (Section 3.4). The corresponding time is similar to the value found for flow adjustment from obstacle-resolving microscale model results, which was determined to “a few minutes” by Schlünzen *et al.* (2011). With the nudging coefficient  $5 \times 10^{-3} \text{ s}^{-1}$ , wind speeds at obstacles are reduced, but the nudging effects are not too strong and additionally depend on the weighting function.

For the weighting function, we used two urban canopy parameters: building surface fraction and building height. Building surface fraction (*bsf*) is defined as the ratio of the building plan area to total plan area. In the current study, *bsf* of each grid refers to the fraction of subgrid-scale buildings within a grid volume. *bsf* is a three-dimensional array and the values are between 0 and 1, varying with space. The value of *bsf* for one grid column changes with height and reaches zero above the height of the tallest building. This means this approach is considered up to the height of the highest obstacle at a grid cell at place  $(x, y)$  starting from the surface. Then the weighting function is defined as

$$\mathcal{W}(x, y, z) = \text{bsf}(x, y, z). \quad (4)$$

Note that  $\text{bsf}(x, y, z)$  is zero without any buildings in the corresponding grid volume  $(x, y, z)$ . With the parameter *bsf*, nudging is only active for the grid cell with subgrid-scale land-cover class belonging to an urban class, and the grid cell is partially or totally covered by obstacles.

The nudging approach is similar to the drag-force approach, which also adds a diffusion term to the right-hand side of the conservation of momentum equation (Brown, 2000; Martilli *et al.*, 2002). As the diffusion terms in both the nudging approach and the drag-force approach contain height-dependent weighting functions, both approaches are height-dependent from the ground up to the highest building, and proportional to the fractional area of the buildings. The difference between these two approaches is that the former is a purely mathematical linear diffusion term while the latter is a nonlinear term ( $\sim U^2$ ) and has physical meaning.

One challenge to overcome is that nudging does not conserve energy, that is, kinetic energy is lost at each time step by nudging winds. To overcome this problem, the lost kinetic energy is firstly tracked and then added back to the right-hand side of the subgrid-scale TKE equation as a source term at each time step and each model level.

At the lowest atmospheric model level ( $z = 10 \text{ m}$ ), the subgrid-scale TKE at time step  $n + 1$ ,  $\bar{e}^{n+1}$ , is calculated in differential form as

$$\bar{e}^{n+1} = \frac{(u_*^{n+1})^2}{c_1^2} + \underbrace{G^{n+1}}_{\text{Energy from the nudging terms}}, \quad (5a)$$

$$G^{n+1} = \frac{1}{2} \rho_0 \alpha^* \left\{ \left[ (\bar{u}^{n+1})^2 + (\bar{v}^{n+1})^2 + (\bar{w}^{n+1})^2 \right] - \left[ (\bar{u}^n)^2 + (\bar{v}^n)^2 + (\bar{w}^n)^2 \right] \right\}, \quad (5b)$$

where  $u_*^{n+1}$  is the friction velocity at time step  $n + 1$ , and  $c_1$  is the proportionality constant.  $\bar{u}^{n+1}$ ,  $\bar{v}^{n+1}$ ,  $\bar{w}^{n+1}$ , and  $\bar{u}^n$ ,  $\bar{v}^n$ ,  $\bar{w}^n$  are the Reynolds-averaged wind-velocity components at time step  $n + 1$  and  $n$ , respectively. The original equation  $\bar{e}^{n+1} = (u_*^{n+1})^2 / c_1^2$  ensures continuous fluxes (Schlünzen *et al.*, 2018). The additional  $G^{n+1}$  term is the energy resulting from the nudging term, calculated by Equation 5b, at time step  $n + 1$ , which is the kinetic energy change between time steps  $n + 1$  and  $n$ . It is added to the TKE equation, thus the  $G$  term represents the energy conversion of mean kinetic energy into turbulence kinetic energy  $\bar{e}$  generated by the interactions between buildings and the airflow.

Above  $z = 10 \text{ m}$ , where the first model level is located, the  $G$  term is added to the prognostic equation of the subgrid-scale TKE as follows:

$$\begin{aligned} \frac{\partial \rho_0 \alpha^* \bar{e}}{\partial t} = & \underbrace{- \frac{\partial \bar{u}_j \rho_0 \alpha^* \bar{e}}{\partial x_j}}_{\text{Advection}} \\ & + \underbrace{\rho_0 \alpha^* \left( K_{ij} 2S_{ij} - \frac{2}{3} \delta_{ij} \bar{e} \right) \frac{\partial \bar{u}_j}{\partial x_j} - \frac{\partial}{\partial x_j} \left( \rho_0 \alpha^* K_{j,x} \frac{\partial \bar{e}}{\partial x_j} \right)}_{\text{Transport term}} \\ & - \underbrace{\rho_0 \alpha^* \frac{g}{\theta_0} K_{3,x} \left( \frac{\partial \bar{\theta}}{\partial z} - \Gamma_\theta \right) - \rho_0 \alpha^* g \cdot 0.61 K_{3,x} \left( \frac{\partial \bar{q}}{\partial z} - \Gamma_q \right)}_{\text{Temperature and humidity-related production}} \\ & - \underbrace{\rho_0 \alpha^* \varepsilon}_{\text{Dissipation}} + \underbrace{G}_{\text{Energy from the nudging terms}}. \end{aligned} \quad (6)$$

Here  $\bar{e} = 0.5 \sum_{i=1}^3 u_i' u_i'$  is the mean TKE,  $i$  and  $j$  are indices taking values of 1, 2, and 3 for the three Cartesian coordinates  $(x, y, z)$ , respectively;  $K_{ij}$  is the turbulent exchange

coefficient for momentum in the  $x_j$  direction;

$$S_{ij} = \frac{\partial \bar{u}_i}{\partial \bar{x}_j} + \frac{\partial \bar{u}_j}{\partial \bar{x}_i},$$

$\delta_{ij}$  denotes the Kronecker delta;  $K_{3,\chi}$  is the vertical exchange coefficient for the scalar variable  $\chi$ .  $K_{3,\chi}$  depends on the mixing length, the Richardson number, and TKE.  $\Gamma_q$  and  $\Gamma_\theta$  are the potential temperature countergradient and humidity countergradient terms, respectively, active for convective atmospheric conditions (Lüpkes and Schlünzen, 1996). The term  $G$  represents the canopy-induced TKE source.

Thus, parameterization using a nudging approach consists of three main steps: (1) nudge winds; (2) track the lost kinetic energy due to wind-nudging; (3) add the lost kinetic energy as a source term to the turbulence kinetic energy equation. A workflow is provided in Figure S1 in the Supporting Information.

### 3 | COMPARISON DATA AND MODEL SETUP

#### 3.1 | Meteorological microscale comparison data

To evaluate the urban canopy parameterization effects, observation data from meteorological stations are usually used: for example, the Basel Urban Boundary Layer Experiment (BUBBLE) microclimate field campaign conducted in the city of Basel (Christen and Vogt, 2004; Rotach *et al.*, 2005; Moradi *et al.*, 2021). However, for the current assessment, spatial average profiles over different types of canopies were needed. In this context, the data of a Reynolds-averaged Navier–Stokes (RANS) based obstacle-resolving microscale model, which captures well the detailed characteristics of urban winds and turbulent flows at multiple levels above and within urban canopies, provide an optimal choice to be used for the validation datasets. In addition, previous studies showed that RANS models can simulate urban flow fields accurately and are commonly used for microscale applications (Hertwig *et al.*, 2012; Grawe *et al.*, 2013a). Thus, in the current study, the published simulation results of the Microscale Transport and Stream model (MITRAS) are used for model evaluation.

MITRAS is the sister model of METRAS. It is a three-dimensional, nonhydrostatic, prognostic, numerical model for wind, temperature, and humidity (Schlünzen *et al.*, 2003; Grawe *et al.*, 2013a; Salim *et al.*, 2018). Obstacles (buildings, trees, etc.) are resolved explicitly in MITRAS using the building-mask concept. MITRAS has

been developed based on METRAS, and both models share many properties and parameterizations. For example, Monin–Obukhov similarity theory is assumed in the lowest model layer, and exchange coefficients above the lowest model layer are calculated using Prandtl–Kolmogorov closure.

The simulated microscale domain is described in Section 3.2. Vertically, the microscale model domain has 91 levels reaching 8,587 m above ground, with the lowest model level at 2.5 m above ground. The vertical resolution increases above 150 m nonequidistantly from 5 m to 200 m at the top of the model domain. Horizontal wind, vertical wind, and TKE are calculated as influenced by obstacles. Results are stored for all grid cells every 5 min (Voss, 2023) and are analysed as given in Section 4.

#### 3.2 | Building data for the parameterization

The parameterization is tested for the central urban area of Hamburg (Germany). The 3D city model LoD2 (Level of Detail 2) Hamburg, which contains building information, serves as input data. A microscale model domain covering 2.88 km<sup>2</sup> in the city centre of Hamburg is used. This domain includes different urban complexity, in terms of building-height variability, elements of urban composition (e.g., Elbe River, Inner Alster Lake), and street patterns (Salim *et al.*, 2015). It has 730 × 730 grid cells with a horizontal resolution of 2.5 m. Buildings in the domain are between 10 m (about 2.0% of all buildings) and 140 m high, and the average value of the building height,  $H_r$ , is 35.24 m.

To understand better the spatial distribution of building coverage over the model domain, we separated the centre area of the model domain (hereafter  $Di$ , note that  $Di$  has 600 × 600 grid cells) into nine equally sized subdomains (hereafter  $Di1$ – $Di9$ ), each having 200 × 200 grid cells and covering an area of 0.25 km<sup>2</sup> (Figure 1). We then calculated the building surface fraction for each subdomain and at different height intervals: 0–20, 20–40, 40–60, 60–80 m. These four height intervals correspond to the first four vertical layers in METRAS (lower to upper level of the corresponding layer). As the building surface fraction, information from  $Di$  is used to determine the weighting function for the nudging simulation in METRAS.

The distributions of building heights and building surface fractions in the nine subdomains show both clear differences and similarities (Figure 2). For example,  $Di8$ , which is mostly covered by Inner Alster Lake (Figure 1), has the lowest building coverage (Figure 2).  $Di4$ – $Di7$  are covered by higher and denser buildings compared with other subdomains. The average building heights of the nine subdomains are in the range 31.6 m ( $Di1$ ) to

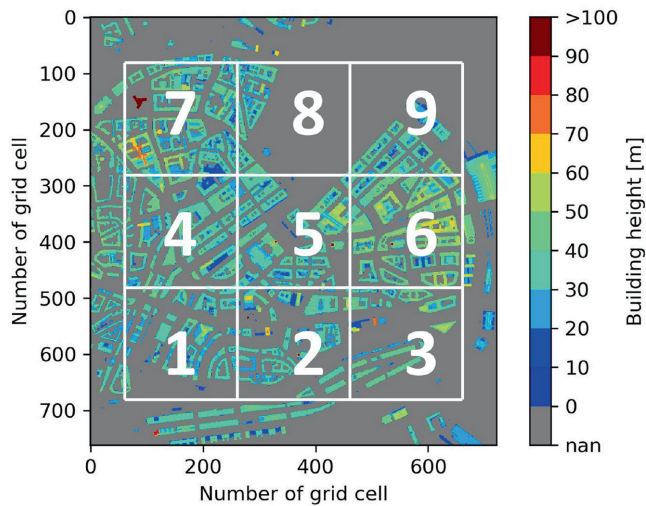


**FIGURE 1** Spatial distribution of building heights in the microscale model domain and schematic illustration of centre area ( $D_i$ ) division into nine subdomains ( $D_{i1}$ – $D_{i9}$ ). The whole domain  $D_i$  has a 2.5-m horizontal resolution and covers 2.88 km<sup>2</sup>. Each subdomain has 200 × 200 grids and covers 0.25 km<sup>2</sup>. Grey spaces denote water, sealed, or other open areas that are not covered by obstacles. [Colour figure can be viewed at [wileyonlinelibrary.com](http://wileyonlinelibrary.com)]

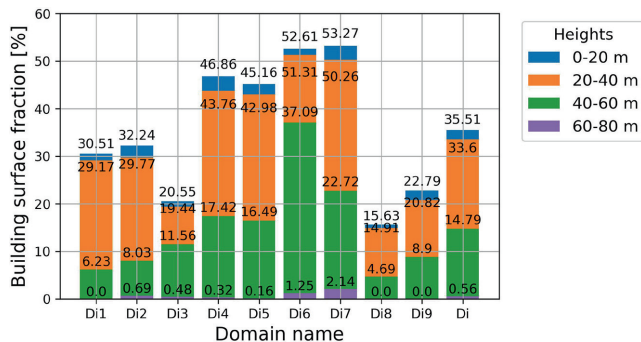


**FIGURE 2** Stacked bar chart of building surface fraction at different height levels for each subdomain  $D_{i1}$ – $D_{i9}$  and for the microscale model domain  $D_i$ . Choice of height level is based on the vertical layers in mesoscale model METRAS. [Colour figure can be viewed at [wileyonlinelibrary.com](http://wileyonlinelibrary.com)]

41.2 m ( $D_{i6}$ ). The highest building with 140 m is located in  $D_{i2}$ . Note that orography is neglected for the present study.

The simulations were carried out for idealized meteorological conditions (Voss, 2023) summarized in Table 1 (column MITRAS). A diurnal cycle was not simulated, and thus only the dynamic effect of the buildings is studied. Wind fields and turbulence kinetic energy values were analysed for the evaluation (Section 4); these are available at a 2.5-m horizontal and 5-m vertical resolution within the canopy layer.

### 3.3 | Mesoscale model setup

Based on the microscale model domain  $D_i$ , we developed a mesoscale model domain (hereafter  $D_e$ ) for the model METRAS. The domain  $D_e$  covers 15 × 15 km<sup>2</sup> with 30 × 30 grid cells and has a horizontal resolution of 500 m. The nine grid cells ( $D_{e1}$ – $D_{e9}$ ) located in the domain centre represent the nine subdomains  $D_{i1}$ – $D_{i9}$  (Figure 3). The vertical resolution is 20 m near the surface, with the lowest model level at 10 m, and increases above 80 m from 20 to 1,000 m vertical resolution at the top of the model domain at 12 km height. “Grass” fully covers the whole domain, except for the nine urbanized centre grid cells. As subgrid-scale land cover is allowed in METRAS, the nine centre grid cells are partially covered by the “compact sealed urban” and “grass” surface land cover classes. The subgrid-scale surface cover fraction for the urban class is determined using the *bsf* values from 0–20 m (Figure 2). The values for weighting functions in the nudging term for each urban grid cell at each vertical level in  $D_e$  are identified using *bsf* calculated from  $D_i$  (Figure 3). The urbanized part in the model domain is admittedly very small. This size was deliberately chosen to assess whether the present nudging approach influences the model results sufficiently towards a more realistic simulation of the wind field within the urban canopy, even if the model grid size is coarse compared with the extension of the urban area.

As the MITRAS simulation was carried out for idealized conditions (Voss, 2023), the METRAS simulations are carried out for the same idealized meteorological conditions. The values of input parameters are listed in Table 1. The ambient temperature is set to 283 K at the surface and changes with height according to the potential temperature gradient of 0.005 K·m<sup>−1</sup>, which represents a stable atmospheric stratification. The diurnal cycle for temperature is not taken into account to study purely aerodynamic effects and their changes induced by nudging. Both simulations start at 04:00 am local standard time (LST); MITRAS is integrated for 70 min, while METRAS is integrated for 30 hr to assess possible longer term influences of the nudging. For comparison analysis, only the outputs from 04:00–04:45 am LST are presented, since results change very little in the remaining time (not shown).

### 3.4 | Sensitivity study of nudging coefficient $\delta$

Values of the nudging coefficient  $\delta$  usually have to be selected empirically. We have conducted sensitivity experiments to assess how sensitive simulation results are to changes of the nudging coefficient.  $\delta$  was set to  $5 \times 10^{-1}$ ,

**TABLE 1** Input parameters for this study, meteorological conditions in MITRAS and METRAS simulations.

Variables	MITRAS	METRAS
Simulation time	04:00–05:10 am LST	04:00 am LST–10:00 am LST next day
Undisturbed wind speed from west at the model top		3.0 m·s <sup>-1</sup>
Temperature at the surface		283 K
Potential temperature gradient		0.005 K·m <sup>-1</sup>
Surface pressure		1,013 hPa
Diurnal cycle		No

Abbreviation: LST, local standard time.

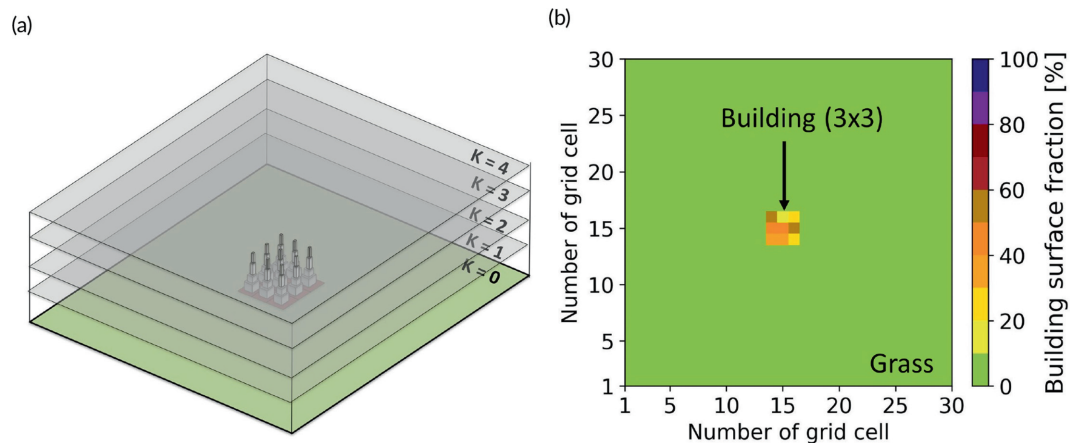


**FIGURE 3** (a) 3D illustration and (b) horizontal cross-section of the mesoscale model domain *De*. The building area covers 3 × 3 grid cells, grass covers 30 × 30 grid cells. [Colour figure can be viewed at [wileyonlinelibrary.com](http://wileyonlinelibrary.com)]

$5 \times 10^{-2}$ ,  $5 \times 10^{-3}$ , and  $5 \times 10^{-4} \text{ s}^{-1}$ . Considering the average value of *bsf* over the nine urban grid cells from 0–20 m of 0.3551 (Figure 2, column Di), the characteristic time  $1/(\delta \cdot bsf)$  in the urban grid cells for each case is about 5 s for  $\delta = 5 \times 10^{-1} \text{ s}^{-1}$ , 1 min for  $\delta = 5 \times 10^{-2} \text{ s}^{-1}$ , 10 min for  $\delta = 5 \times 10^{-3} \text{ s}^{-1}$ , and 100 min for  $\delta = 5 \times 10^{-4} \text{ s}^{-1}$ .

Figure 4 shows results for the temporal development of the spatially averaged wind profiles over the nine urban grid cells (*De1–De9*) in METRAS. For  $\delta = 5 \times 10^{-1}$  and  $5 \times 10^{-2} \text{ s}^{-1}$ , in less than 5 min wind profiles are close to a steady state; however, there is almost no wind in the urban canopy layer, which indicates that the nudging effects are too strong (Figure 4a,b). Considering the average *bsf* of below 36%, light winds are to be expected in the canopy. For  $\delta = 5 \times 10^{-3} \text{ s}^{-1}$ , the wind profiles are relatively steady within about 10 minutes as expected, and the nudging effects are neither too strong nor too weak (Figure 4c). In addition, the value  $5 \times 10^{-3} \text{ s}^{-1}$  also reflects the adjustment time of about 4 min obtained in the obstacle-resolving microscale model for the wind (and temperature) profiles, as shown in figure 4 of Schlünzen *et al.* (2011). For  $\delta = 5 \times 10^{-4} \text{ s}^{-1}$ , the wind profile after 45 min is still almost the same as the basic state, which means nudging has

nearly no impact on wind velocities (Figure 4d). Thus,  $\delta$  is set to  $5 \times 10^{-3} \text{ s}^{-1}$ .

## 4 | COMPARISON BETWEEN METRAS AND MITRAS DATA

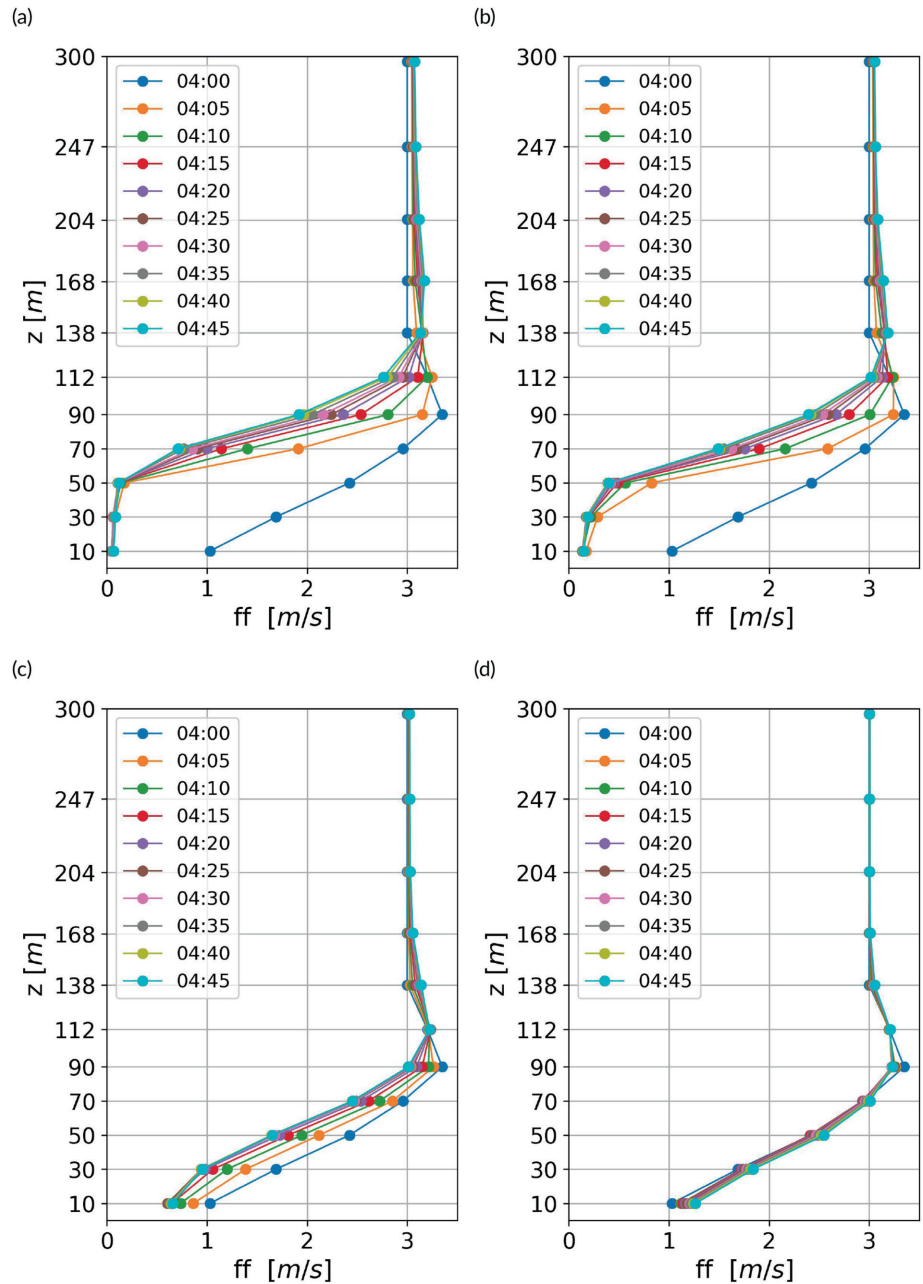
In this section, a comparison between METRAS model results (with and without nudging) and MITRAS data is made for wind speeds and turbulence kinetic energy. We first compare results for the whole urban area (*De* and *Di*), then we go into details for each urban subdomain (*De1–De9* and *Di1–Di9*).

### 4.1 | Results over the whole urban area

Figure 5a presents a comparison between the vertical profiles of horizontally averaged wind speeds over the nine urban grid cells obtained from the METRAS run with nudging (METRAS-nud) and the average profile over the nine subdomains obtained from the MITRAS run (MITRAS). Results of the METRAS run but without using



**FIGURE 4** Temporal development of spatially averaged wind profiles over the nine urban grids (*De1–De9*) using METRAS for an integration starting at 04:00 am LST (basic state) and encompassing the following 45 min. Simulations are carried out for the same initial meteorological conditions but with different values of the nudging coefficient: (a)  $\delta = 5 \times 10^{-1}$ , (b)  $\delta = 5 \times 10^{-2}$ , (c)  $\delta = 5 \times 10^{-3}$ , and (d)  $\delta = 5 \times 10^{-4} \text{ s}^{-1}$ . [Colour figure can be viewed at [wileyonlinelibrary.com](http://wileyonlinelibrary.com)]



the nudging approach (METRAS-nonud) are added for comparison. Note that, even though there are more vertical levels in the MITRAS model domain than in the METRAS model domain, MITRAS simulation results are chosen only at the mesoscale vertical layers for this comparison analysis, that is, 10, 30, 50, 70, 90, 112, 138, 168, 204, 247, 300 m. If the microscale vertical level is not consistent with the mesoscale vertical level, nearest-neighbour interpolation is used.

Figure 5a shows that wind profiles obtained from both METRAS-nud and METRAS-nonud peak at 90 m high. From 10 to 70 m, wind speeds of METRAS-nud and MITRAS show good agreement, suggesting that the nudging approach performs well in representing wind-blocking

effects in the canopy layers if appropriate values are used for the forcing field (here: zero wind speed) and the weighting function. Compared with METRAS-nonud, wind speeds of METRAS-nud and MITRAS are approximately 30% lower.

At the levels above 90 m ( $z > 2.5Hr$ , note that  $Hr$  is the average building height), vertical profiles of both METRAS-nud and METRAS-nonud runs overlap almost completely, indicating that the influences of obstacles on the mean flow apply only up to the level  $z \approx 2.5Hr$  and the airflow is fully adjusted to the underlying surface above this height. This is consistent with a previous study in which horizontal homogeneity of the urban canopy flow is achieved at 2–5 times the average building height

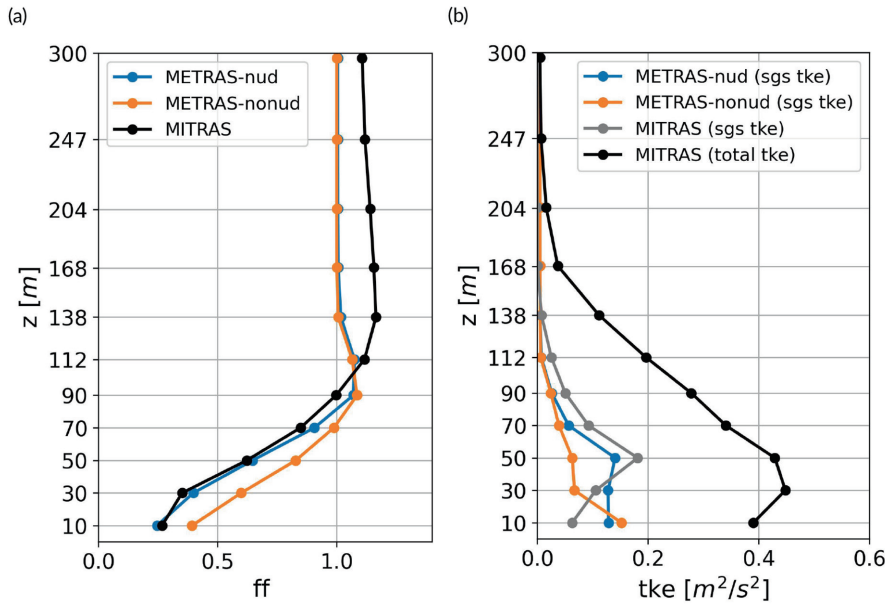


**FIGURE 5** Vertical profiles of horizontally averaged (a) horizontal wind velocity  $ff$  and (b) subgrid-scale TKE ( $tke$ ).  $ff$  is normalized by the undisturbed wind speed (Table 1). The blue line represents the METRAS simulation with nudging (METRAS-nud), the yellow line the METRAS simulation without nudging (METRAS-nonud), and the black line the MITRAS simulation. For TKE, the black line represents the total TKE obtained from the MITRAS simulation result (MITRAS (total tke)), the grey line subgrid-scale TKE obtained from the MITRAS simulation result (MITRAS (sgs tke)). [Colour figure can be viewed at [wileyonlinelibrary.com](http://wileyonlinelibrary.com)]

(Raupach *et al.*, 1991). However, these two vertical profiles above 90 m are quite different from the MITRAS run, that is, wind speeds of METRAS-nud and METRAS-nonud are lower than those of MITRAS. The reason for this is that buildings are resolved explicitly in the microscale model MITRAS and vortices caused by buildings are stronger in MITRAS than METRAS. Moreover, besides horizontal transport, large momentum transport from lower to upper levels and vice versa occurs in MITRAS. That is, updraft and downdraft vertical velocities are higher in MITRAS than METRAS-nud and METRAS-nonud (Figure S2 in the Supporting Information).

For comparing TKE with METRAS and MITRAS, two terms are distinguished: the resolved TKE and the subgrid-scale TKE. The resolved TKE ( $TKE_{RES}$ ) is calculated from the output velocity fields at each microscale model grid point  $i$ , given by Equation 7:

$$\begin{aligned}
 TKE_{RES}(t) &= \frac{1}{n} \sum_{i=1}^n \frac{\hat{u}_i(t)^2 + \hat{v}_i(t)^2 + \hat{w}_i(t)^2}{2} \\
 &= \frac{1}{n} \sum_{i=1}^n \frac{(\bar{u}_i(t) - \langle \bar{u}(t) \rangle)^2 + (\bar{v}_i(t) - \langle \bar{v}(t) \rangle)^2 + (\bar{w}_i(t) - \langle \bar{w}(t) \rangle)^2}{2},
 \end{aligned}
 \quad (7)$$

where the resolved velocity deviations  $\hat{u}_i(t)$ ,  $\hat{v}_i(t)$ ,  $\hat{w}_i(t)$ , are calculated at each grid point  $i$  as the differences between the instantaneous velocities at this grid point,  $\bar{u}_i(t)$ ,  $\bar{v}_i(t)$ ,  $\bar{w}_i(t)$  (note that the overbars here refer to the Reynolds averaging as in Equations 3, 5, 6) and the horizontally averaged velocities,  $\langle \bar{u}(t) \rangle$ ,  $\langle \bar{v}(t) \rangle$ ,  $\langle \bar{w}(t) \rangle$ , respectively.

The parameterized subgrid-scale TKE ( $TKE_{SGS}$ ) is calculated directly by the corresponding model. As mentioned above, for the current study, Prandtl–Kolmogorov closure solving a prognostic equation for  $TKE_{SGS}$  is employed in both METRAS and MITRAS models. The sum

of  $TKE_{RES}$  and  $TKE_{SGS}$  is the total TKE ( $TKE_{TOT}$ ):

$$TKE_{TOT} = TKE_{RES} + TKE_{SGS}. \quad (8)$$

Figure 6 illustrates the relationship between the TKE for a mesoscale grid and the TKE for a microscale grid system. For a single mesoscale grid (Figure 6a), the TKE of the eddies smaller than the model grid size is  $TKE_{SGS}$  (blue arrows). Assuming that the mesoscale grid consists of  $4 \times 4$  microscale grid cells (Figure 6b), the amount of  $TKE_{SGS}$  for a single mesoscale grid should be approximately equal to  $TKE_{TOT}$  of the corresponding  $4 \times 4$  microscale grids, which is the sum of  $TKE_{RES}$  and the averaged  $TKE_{SGS}$  over all  $4 \times 4$  microscale grids. In the present study,  $TKE_{SGS}$  obtained from METRAS and MITRAS is averaged over the domains  $De$  and  $Di$ , respectively. As the nine urban grid cells in the mesoscale model domain  $De$  represent the nine subdomains of  $Di$ , the averaged  $TKE_{SGS}$  over the nine urban grid cells in  $De$  should be approximately equal to the averaged  $TKE_{TOT}$  over the whole domain  $Di$  (note that for METRAS nine grid cells are in the domain  $De$ , while for MITRAS there are 360,000 cells in the domain  $Di$ ).

Figure 5b shows vertical profiles of the horizontally averaged  $TKE_{SGS}$  obtained from the METRAS-nud and METRAS-nonud runs, and the  $TKE_{SGS}$  and  $TKE_{TOT}$  obtained from the MITRAS run. It was found that simulated  $TKE_{SGS}$  in both METRAS-nud and MITRAS runs reaches maximum values at 50 m high ( $z \approx 1.4Hr$ , just above the mean building height) and reaches zero at about 138 m high ( $z \approx 3.9Hr$ ). This is similar to the results obtained in a wind-tunnel study by Kastner-Klein and Rotach (2004), who modelled and measured turbulence structures within and above a realistic urban canopy with

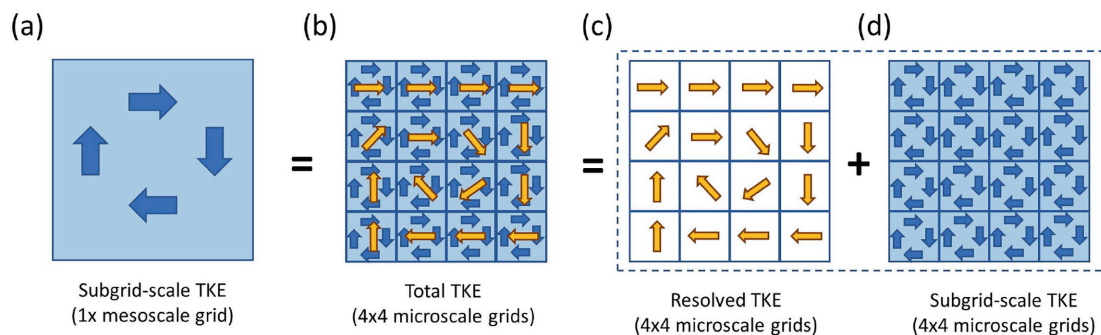


**FIGURE 6** Schematic illustration of the relationship between the subgrid-scale TKE of (a) a mesoscale grid and (b–d) the total TKE of microscale grids assuming that the mesoscale grid consists of  $4 \times 4$  microscale grid cells. The yellow arrows denote large eddies that can be resolved by the microscale model. The blue arrows in the mesoscale and microscale grids denote small eddies that cannot be resolved directly in mesoscale and microscale models, respectively. [Colour figure can be viewed at [wileyonlinelibrary.com](http://wileyonlinelibrary.com)]

highly variable building heights and shapes and found that the maximum values of TKE occurred at 1–1.5 times the average roof level.

At 10 m above ground, the  $TKE_{SGS}$  of METRAS-nud is slightly lower than that of METRAS-nonud. The reason for this is that  $TKE_{SGS}$  is related to wind speed, and wind speeds of METRAS-nud at 10 m are reduced due to nudging. At 10–112 m,  $TKE_{SGS}$  of METRAS-nud is above the values achieved without nudging (METRAS-nonud). Compared with  $TKE_{SGS}$  of the MITRAS run, more  $TKE_{SGS}$  is obtained from the METRAS-nud run at 50 m above ground, which indicates that the parameterization induces some of the canopy-induced TKE. However, above 50 m high, the  $TKE_{SGS}$  of METRAS-nud is below that of MITRAS. In addition, when comparing  $TKE_{SGS}$  of METRAS-nud with  $TKE_{TOT}$  obtained from the MITRAS run, the latter has much higher values than the former within and above canopies. This indicates that the nudging parameterization underestimates canopy-induced TKE and an extra source of TKE is required. Two main reasons could cause this underestimation. First, the resolved buildings in MITRAS cause more surround-building vertical vortices, thus more TKE is produced. Secondly, the subgrid-scale urban spatial heterogeneity including building-height variation and street patterns is not represented in the nudging parameterization used for the mesoscale model domain. The turbulence caused by the complex buildings in the airflow is thus only partly represented by the nudging approach, where the kinetic energy lost by nudging is added to  $TKE_{SGS}$ .

## 4.2 | The impacts of building surface fraction on airflow

To study the effects of building surface fraction on airflow better, we categorized the subdomains into three

groups based on the values of  $bsf$  at heights of 0–20 m (see Figure 2): *high bsf* ( $Di7$ ,  $Di6$ ,  $Di4$ , and  $Di5$ ), *middle bsf* ( $Di2$  and  $Di1$ ), and *low bsf* ( $Di9$ ,  $Di3$ , and  $Di8$ ). Figure 7 shows vertical profiles of horizontally averaged wind speeds over each subdomain in  $Di$  from the MITRAS run (Figure 7a) and for the same domain from the METRAS-nud run (Figure 7b) at all corresponding grid levels. Results from the MITRAS run show that averaged wind speeds of each subdomain for lower altitudes below  $\sim 50$  m are related to the building surface fraction, while wind speeds of the *high bsf* group ( $Di7$ ,  $Di6$ ,  $Di4$ ,  $Di5$ ) are lower than those of the *middle* ( $Di2$  and  $Di1$ ) and *low bsf* ( $Di9$ ,  $Di3$ , and  $Di8$ ) groups. In general, *higher bsf* results in lower wind speeds within the canopy (Figure 7a). However, due to the vertical momentum transport (Figure S3 in the Supporting Information), this signal is not pronounced at higher latitudes above  $\sim 50$  m. In contrast to the high spatial variation in wind speeds of the nine subdomains from the microscale model results, Figure 7b shows that wind speeds of the corresponding nine mesoscale urban grids in  $De$  do not vary greatly. The reason for that might be that all nine urban grid cells are closely located and the effects from neighbouring grids are strong. For example,  $Di5$  belongs to the *high bsf* group but has the lowest wind speeds, due to its location in the centre of the domain. With an urban area of  $3 \times 3$  grid points, the relatively small spatial differences are not surprising, keeping in mind that “... 5–8 grid lengths is the scale of the atmospheric process that is captured by a model” (WMO, 2023). Thus, the effect of flow reduction is represented, but, as to be expected, the heterogeneity cannot be reproduced.

Figure 8 shows the vertical profiles of the horizontally averaged  $TKE_{SGS}$  over the nine subdomains in  $Di$  and  $TKE_{SGS}$  of each corresponding urban grid cell  $De$ . It is evident that the profiles are influenced by building surface fraction (Figure 8a).  $Di6$  with the highest  $bsf$

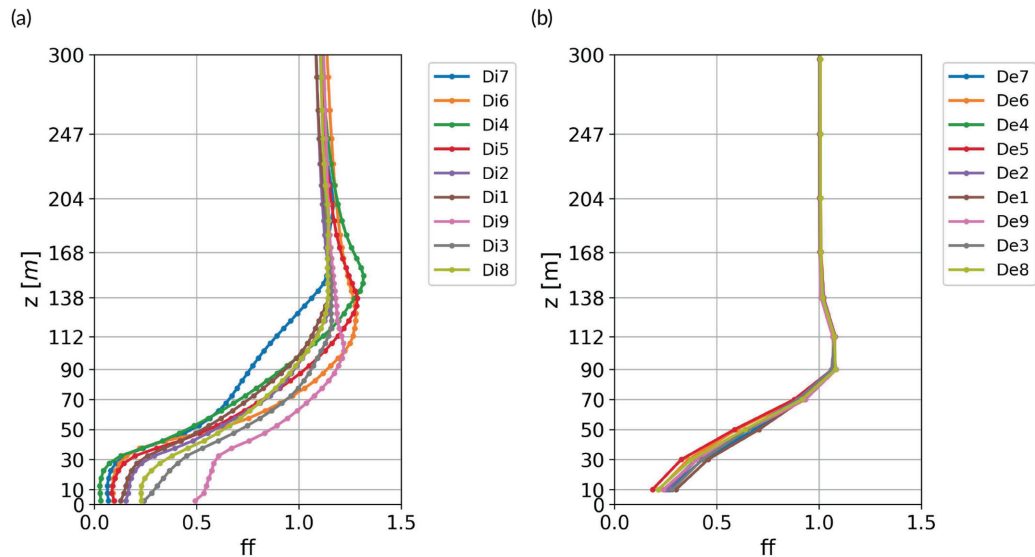


**FIGURE 7** Vertical profiles of horizontally averaged wind velocity ( $ff$ ) for each subdomain from (a) MITRAS ( $Di$ ) and (b) METRAS ( $De$ ).  $ff$  is normalized by the wind speeds in the free atmosphere. Labels are sorted according to the building surface fraction at heights of 0–20 m for each subdomain in  $Di$ , from highest ( $Di7$ ) to lowest ( $Di8$ ). [Colour figure can be viewed at [wileyonlinelibrary.com](http://wileyonlinelibrary.com)]

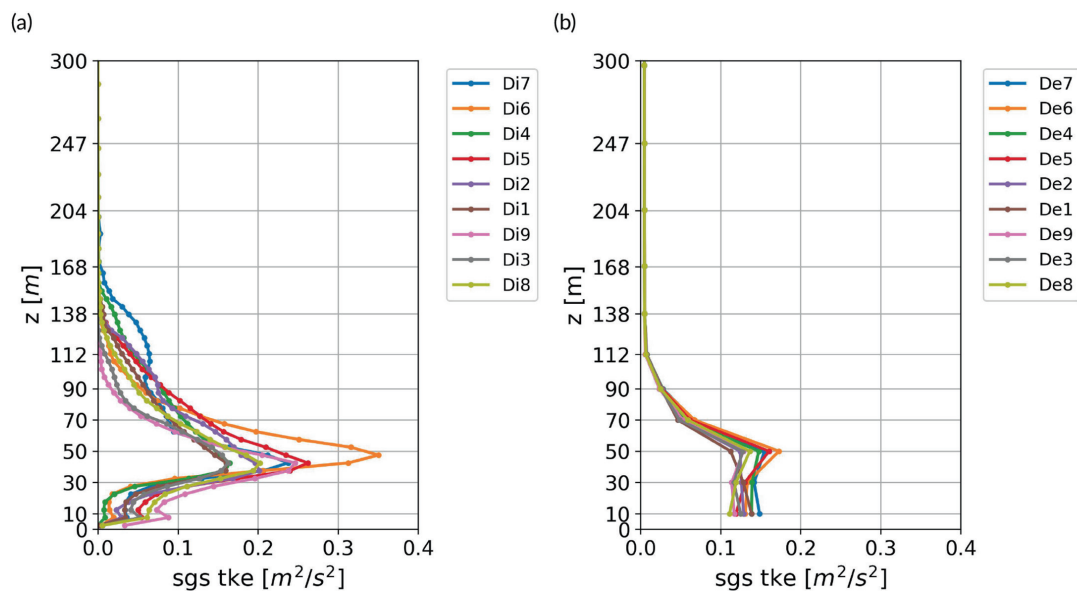


**FIGURE 8** Vertical profiles of horizontally averaged subgrid-scale turbulent kinetic energy ( $sgs\ tke$ ) for each subdomain from (a) MITRAS ( $Di$ ) and (b) METRAS ( $De$ ). Labels are sorted according to the building surface fraction at heights of 0–20 m for each subdomain in  $Di$ , from highest ( $Di7$ ) to lowest ( $Di8$ ). [Colour figure can be viewed at [wileyonlinelibrary.com](http://wileyonlinelibrary.com)]

(0.51) at 20–40 m above ground has higher  $TKE_{SGS}$  compared with other subdomains (Figure 8a,b). In addition, it is worth noting that  $TKE_{SGS}$  from the MITRAS simulation reaches a maximum between 30 and 50 m (between about 1.0 and 1.5  $z/Hr$ ). However, this pattern cannot be seen in Figure 8b, due to the coarser vertical resolution in METRAS.

Moreover, the MITRAS result (Figures 7a and 8a) shows that the impacts of urban heterogeneity on the

mean flow and turbulence kinetic energy distributions are clearly noticeable up to about 168 m ( $z \approx 5Hr$ ), which is higher than  $z \approx 3Hr$  mentioned in the study by Kastner-Klein and Rotach (2004). Above 168 m, the spatial variation in mean velocity and turbulence kinetic energy is less than 15% and 2%, respectively. However, the METRAS-nud result (Figures 7b and 8b) shows that the influences of urban heterogeneity are pronounced only up to 90 m ( $z \approx 2.5Hr$ ).

## 5 | DISCUSSION AND CONCLUSIONS

It is important to take canopy-layer influences on wind and turbulence into account when simulating meteorological fields in urban areas with mesoscale models. The main objective of our study is to show the possibilities and limitations of using the nudging approach as an urban canopy parameterization. The parameterization is novel in terms of its simplicity and efficiency to represent the effects of urban canopies on airflow, that is, the canopy-induced momentum sink, and partly provides a turbulence kinetic energy source. The simplicity of this parameterization allows it to be tested, evaluated, and then implemented further in other high-resolution atmospheric models, such as COSMO, WRF, MM5, and so forth.

To overcome one of the main drawbacks of nudging, that it does not conserve energy, we track the lost kinetic energy and add the amount of energy into the TKE equation as a source term. It is shown that TKE production is represented. However, TKE is still underestimated compared with the model results of the obstacle-resolving model MITRAS. This suggests that an explicit obstacle-induced source of TKE should be included in addition to the conversion of mean kinetic energy to TKE, which, however, would depart from the concept of a simple nudging parameterization and might make it less attractive for use as a simple canopy parameterization in mesoscale and global scale models. In addition, results also show that the vertical turbulent transport is not reflected well by the parameterization. We suggest that the relevance of enhanced vertical transport needs to be assessed in evaluations for realistic cases (e.g., hind-cast of an urban heat island situation for a moderate wind situation and comparison with measurements).

One particular challenge in urban modelling studies is to deal with the relationship between the real complexity of urban morphology and the simplified morphology adopted in the parameterization (Martilli *et al.*, 2015). Two parameters, namely building height and building surface fraction, are used in the current parameterization. Comparison results show that the parameterization using these two parameters can represent aerodynamic effects well. However, the underestimation of TKE might be related to the simplification of urban morphology. At this point, more parameters may be needed to define the simplified morphology. Ching *et al.* (2018) have summarized the common urban canopy parameters required for urban climate modelling, such as building frontal density, vegetation fraction, street orientations, and so forth. Nowadays there are more high-resolution urban morphological datasets available for many cities in the world. For example, the Urban Atlas data developed by European Environment

Agency (EEA) (2018) contains building-height information with 10-m resolution and street tree information in major cities in Europe. In addition, the Local Climate Zone (LCZ) characterizes urban landscapes by a range of urban morphological and physical parameters (Stewart and Oke, 2012). Using the LCZ classification framework, the World Urban Database and Access Portal Tools (WUDAPT) project has characterized many cities around the world in a consistent way and developed the corresponding LCZ maps (Ching *et al.*, 2018). A study by Demuzere *et al.* (2022) has developed the global LCZ dataset with a resolution of 100 m. Researchers need to investigate, using obstacle-resolving models, what influence the class ranges have on spatially averaged microscale model results and whether this is comparable with the simplifications inherent in the current simple nudging approach with TKE source.

For further implementations of the parameterization in various models, it might be necessary to verify the characteristic time  $1/(\delta \cdot bsf)$  and ensure numerical stability for the time steps the model uses (Section 2.1). For most high-resolution models, the model time step has a range of several tens of seconds to several minutes, depending on the horizontal grid resolution. For example, the time step (in seconds) for WRF is usually set to approximately six times the horizontal grid resolution (in km); the time step for MM5 is approximately three times the grid resolution (Skamarock *et al.*, 2019), and the time step for METRAS is varied but less than one minute. With these time steps, the characteristic time of nudging should be set accordingly to this range, that is, several minutes. This guarantees that model states are nudged to forcing fields within just a few time steps. Thus, the nudging coefficient  $\delta = 5 \times 10^{-3} \text{ s}^{-1}$  used in this study (corresponding to a characteristic time of, e.g., 3 min for a 100% building-covered model domain) can be used generally for different studies on various models. The value of the weighting function, which is the height-dependent building surface fraction (*bsf*), needs to be adjusted for different urban areas.

Future research might consider possible developments of the nudging coefficient. The nudging term in this study is linear to the wind speed itself. In contrast to that, the traditional drag-force approach (Brown, 2000; Dupont *et al.*, 2004) parameterizes wind reductions by using the drag term with a form of the square of the wind speed, which is physically more correct. Theoretically, one could also use a nudging coefficient dependent on wind speed. We did not try this approach, which demands time-dependent calculation of the coefficient, because it might hinder the nudging implementation as parameterization of urban effects into nonurbanized mesoscale and global-scale models.

From the thermodynamic perspective, cities exert great influence on the local and regional weather and climate, such as the urban heat island (UHI) phenomenon, anthropogenic heat emissions, radiation trapping due to obstacles, and so forth. It is known that the UHI intensity depends on wind speed and is smaller for larger wind speeds (Schlünzen *et al.*, 2010). In the next step, the influence of the current parameterization on thermodynamic effects of cities, for example, UHI, will be investigated in realistic cases including the calculation of temperature, relative humidity, clouds, rain, and diurnal cycles in the simulations. Moreover, further research can investigate whether nudging of temperature and humidity might improve modelling results.

## AUTHOR CONTRIBUTIONS

**Ge Cheng:** conceptualization; formal analysis; visualization; writing – original draft. **K. Heinke Schlünzen:** conceptualization; funding acquisition; supervision; writing – original draft. **David Grawe:** methodology; resources. **Vivien Voss:** resources; validation. **Marcus Thatcher:** investigation; methodology; supervision. **Peter Rayner:** investigation; methodology; supervision.

## ACKNOWLEDGEMENTS

The research was supported by the Deutsche Forschungsgemeinschaft (DFG, German Research Foundation) under Germany's Excellence Strategy–EXC 2037 “CLICCS–Climate, Climatic Change, and Society”, Project Number: 390683824, contributing to the Center for Earth System Research and Sustainability (CEN) of Universität Hamburg. Open Access funding enabled and organized by Projekt DEAL.

## CONFLICT OF INTEREST STATEMENT

The authors declare that they have no conflict of interest.

## ORCID

Ge Cheng  <https://orcid.org/0000-0002-3145-8968>

## REFERENCES

- Arakawa, A. and Lamb, V.R. (1977) Computational design of the basic dynamical processes of the UCLA general circulation model. *Methods in Computational Physics*, 17, 173–265 <https://www.sciencedirect.com/science/article/pii/B9780124608177500094>.
- Bauer, H.-S. and Wulfmeyer, V. (2009) Validation of components of the water cycle in the ECHAM4 general circulation model based on the Newtonian relaxation technique: a case study of an intense winter cyclone. *Meteorology and Atmospheric Physics*, 104, 135–162. <https://doi.org/10.1007/s00703-009-0018-7>.
- Bollmeyer, C., Keller, J.D., Ohlwein, C., Wahl, S., Crewell, S., Friederichs, P., Hense, A., Keune, J., Kneifel, S., Pscheidt, I., Redl, S. and Steinke, S. (2015) Towards a high-resolution regional reanalysis for the European CORDEX domain. *Quarterly Journal of the Royal Meteorological Society*, 141, 1–15 <https://rmets.onlinelibrary.wiley.com/doi/abs/10.1002/qj.2486>.
- Brill, K.F., Uccellini, L.W., Manobianco, J., Kocin, P.J. and Homan, J.H. (1991) The use of successive dynamic initialization by nudging to simulate cyclogenesis during GALE IOP 1. *Meteorology and Atmospheric Physics*, 45, 15–40. <https://doi.org/10.1007/BF01027473>.
- Brown, M.J. (2000) In: Boybeyi, Z. (Ed.) *Urban Parameterizations for Mesoscale Meteorological Models*. Southampton, UK: WIT Press, pp. 193–255.
- Bullock, O.R., Alapaty, K., Herwehe, J.A., Mallard, M.S., Otte, T.L., Gilliam, R.C. and Nolte, C.G. (2014) An observation-based investigation of nudging in WRF for downscaling surface climate information to 12-km grid spacing. *Journal of Applied Meteorology and Climatology*, 53, 20–33 <https://journals.ametsoc.org/view/journals/apme/53/1/jamc-d-13-030.1.xml>.
- Cheng, G. and Schlünzen, K.H. (2023) A conceptual model for a generalized canopy parametrization for atmospheric models. *Quarterly Journal of the Royal Meteorological Society*, 149, 494–514 <https://rmets.onlinelibrary.wiley.com/doi/abs/10.1002/qj.4420>.
- Ching, J., Mills, G., Bechtel, B., See, L., Feddema, J., Wang, X., Ren, C., Brousse, O., Martilli, A., Neophytou, M., Mouzourides, P., Stewart, I., Hanna, A., Ng, E., Foley, M., Alexander, P., Aliaga, D., Niyogi, D., Shreevastava, A., Bhalachandran, P., Masson, V., Hidalgo, J., Fung, J., Andrade, M., Baklanov, A., Dai, W., Milcinski, G., Demuzere, M., Brunsell, N., Pesaresi, M., Miao, S., Mu, Q., Chen, F. and Theeuwes, N. (2018) WUDAPT: an urban weather, climate, and environmental Modeling infrastructure for the Anthropocene. *Bulletin of the American Meteorological Society*, 99, 1907–1924 <https://journals.ametsoc.org/view/journals/bams/99/9/bams-d-16-0236.1.xml>.
- Choi, H.-J., Lee, H.W., Sung, K.-H., Kim, M.-J., Kim, Y.-K. and Jung, W.-S. (2009) The impact of nudging coefficient for the initialization on the atmospheric flow field and the photochemical ozone concentration of Seoul, Korea. *Atmospheric Environment*, 43, 4124–4136 <https://www.sciencedirect.com/science/article/pii/S1352231009004907>.
- Christen, A. and Vogt, R. (2004) Energy and radiation balance of a central European city. *International Journal of Climatology*, 24, 1395–1421 <https://rmets.onlinelibrary.wiley.com/doi/abs/10.1002/joc.1074>.
- Davies, H.C. (1976) A lateral boundary formulation for multi-level prediction models. *Quarterly Journal of the Royal Meteorological Society*, 102, 405–418 <https://rmets.onlinelibrary.wiley.com/doi/abs/10.1002/qj.49710243210>.
- Demuzere, M., Kittner, J., Martilli, A., Mills, G., Moede, C., Stewart, I.D., van Vliet, J. and Bechtel, B. (2022) A global map of local climate zones to support earth system modelling and urban-scale environmental science. *Earth System Science Data*, 14, 3835–3873 [10.5194/essd-14-3835-2022](https://doi.org/10.5194/essd-14-3835-2022).
- Dierer, S. and Schlünzen, K.H. (2005) Influence parameters for a polar mesocyclone development. *Meteorologische Zeitschrift*, 14, 781–792 [10.1127/0941-2948/2005/0077](https://doi.org/10.1127/0941-2948/2005/0077).
- Dierer, S., Schlünzen, K.H., Birnbaum, G., Brümmer, B. and Müller, G. (2005) Atmosphere–sea ice interactions during a cyclone passage investigated by using model simulations and measurements. *Monthly Weather Review*, 133, 3678–3692 <https://journals.ametsoc.org/view/journals/mwre/133/12/mwr3076.1.xml>.

- Dupont, S., Otte, T.L. and Ching, J.K.S. (2004) Simulation of meteorological fields within and above urban and rural canopies with a mesoscale model. *Boundary-Layer Meteorology*, 113, 111–158. <https://doi.org/10.1023/B:BOUN.0000037327.19159.ac>.
- European Environment Agency (EEA). (2018) Urban-Atlas 2018 and Street Tree Layer (STL) 2018. <https://land.copernicus.eu/local/urban-atlas>.
- Garuma, G.F. (2018) Review of urban surface parameterizations for numerical climate models. *Urban Climate*, 24, 830–851 <https://www.sciencedirect.com/science/article/pii/S2212095517300858>.
- Grawe, D., Schlünzen, K.H. and Pascheke, F. (2013a) Comparison of results of an obstacle resolving microscale model with wind tunnel data. *Atmospheric Environment*, 79, 495–509 <https://www.sciencedirect.com/science/article/pii/S1352231013004974>.
- Grawe, D., Thompson, H.L., Salmond, J.A., Cai, X.-M. and Schlünzen, K.H. (2013b) Modelling the impact of urbanisation on regional climate in the greater London area. *International Journal of Climatology*, 33, 2388–2401 <https://rmets.onlinelibrary.wiley.com/doi/abs/10.1002/joc.3589>.
- Grimmond, C., Best, M., Barlow, J., Arnfield, A.J., Baik, J.-J., Baklanov, A., Belcher, S., Bruse, M., Calmet, I., Chen, F., Clark, P., Dandou, A., Erell, E., Fortuniak, K., Hamdi, R., Kanda, M., Kawai, T., Kondo, H., Krayenhoff, S., Lee, S.H., Limor, S.-B., Martilli, A., Masson, V., Miao, S., Mills, G., Moriwaki, R., Oleson, K., Porson, A., Sievers, U., Tombrou, M., Voogt, J. and Williamson, T. (2009) *Urban Surface Energy Balance Models: Model Characteristics and Methodology for a Comparison Study*. Berlin, Heidelberg: Springer Berlin Heidelberg, pp. 97–123. [https://doi.org/10.1007/978-3-642-00298-4\\_11](https://doi.org/10.1007/978-3-642-00298-4_11).
- Hertwig, D., Efthimiou, G.C., Bartzis, J.G. and Leidl, B. (2012) CFD-RANS model validation of turbulent flow in a semi-idealized urban canopy. *Journal of Wind Engineering and Industrial Aerodynamics*, 111, 61–72 <https://www.sciencedirect.com/science/article/pii/S0167610512002474>.
- Hoke, J.E. and Anthes, R.A. (1976) The initialization of numerical models by a dynamic-initialization technique. *Monthly Weather Review*, 104, 1551–1556 [https://journals.ametsoc.org/view/journals/mwre/104/12/1520-0493\\_1976\\_104\\_1551\\_tionmb\\_2\\_0\\_co\\_2.xml](https://journals.ametsoc.org/view/journals/mwre/104/12/1520-0493_1976_104_1551_tionmb_2_0_co_2.xml).
- Källberg, P. (1977) Test of a lateral boundary relaxation scheme in a barotropic model. ECMWF, Research Department, Internal Report, Bracknell, 3.
- Kastner-Klein, P. and Rotach, M.W. (2004) Mean flow and turbulence characteristics in an urban roughness sublayer. *Boundary-Layer Meteorology*, 111, 55–84. <https://doi.org/10.1023/B:BOUN.0000010994.32240.b1>.
- Koopmans, S., van Haren, R., Theeuwes, N., Ronda, R., Uijlenhoet, R., Holtslag, A.A.M. and Steeneveld, G.-J. (2023) The set-up and evaluation of fine-scale data assimilation for the urban climate of Amsterdam. *Quarterly Journal of the Royal Meteorological Society*, 149, 171–191 <https://rmets.onlinelibrary.wiley.com/doi/abs/10.1002/qj.4401>.
- Korsholm, U.S., Petersen, C., Sass, B.H., Nielsen, N.W., Jensen, D.G., Olsen, B.T., Gill, R. and Vedel, H. (2015) A new approach for assimilation of 2D radar precipitation in a high-resolution NWP model. *Meteorological Applications*, 22, 48–59 <https://rmets.onlinelibrary.wiley.com/doi/abs/10.1002/met.1466>.
- Kruse, C.G., Bacmeister, J.T., Zarzycki, C.M., Larson, V.E. and Thayer-Calder, K. (2022) Do nudging tendencies depend on the nudging timescale chosen in atmospheric models? *Journal of Advances in Modeling Earth Systems*, 14, e2022MS003024 <https://agupubs.onlinelibrary.wiley.com/doi/abs/10.1029/2022M%003024>.
- Kumar, V., Chandrasekar, A., Alapaty, K. and Niyogi, D. (2008) The impacts of indirect soil moisture assimilation and direct surface temperature and humidity assimilation on a mesoscale model simulation of an Indian monsoon depression. *Journal of Applied Meteorology and Climatology*, 47, 1393–1412 <https://journals.ametsoc.org/view/journals/apme/47/5/2007jamc1599.1.xml>.
- Liu, J., Yang, S., Ma, L., Bao, X., Wang, D. and Xu, D. (2013) An initialization scheme for tropical cyclone numerical prediction by enhancing humidity in deep-convection region. *Journal of Applied Meteorology and Climatology*, 52, 2260–2277 <https://journals.ametsoc.org/view/journals/apme/52/10/jamc-d-12-0310.1.xml>.
- Lüpkes, C. and Schlünzen, K.H. (1996) Modelling the arctic convective boundary-layer with different turbulence parameterizations. *Boundary-Layer Meteorology*, 79, 107–130. <https://doi.org/10.1007/BF00120077>.
- Martilli, A., Clappier, A. and Rotach, M.W. (2002) An urban surface exchange parameterisation for mesoscale models. *Boundary-Layer Meteorology*, 104, 261–304. <https://doi.org/10.1023/A:1016099921195>.
- Martilli, A., Santiago, J.L. and Salamanca, F. (2015) On the representation of urban heterogeneities in mesoscale models. *Environmental Fluid Mechanics*, 15, 305–328. <https://doi.org/10.1007/s10652-013-9321-4>.
- Masson, V. (2000) A physically-based scheme for the urban energy budget in atmospheric models. *Boundary-Layer Meteorology*, 94, 357–397. <https://doi.org/10.1023/A:1002463829265>.
- Masson, V. (2006) Urban surface modeling and the meso-scale impact of cities. *Theoretical and Applied Climatology*, 84, 35–45. <https://doi.org/10.1007/s00704-005-0142-3>.
- Moradi, M., Dyer, B., Nazem, A., Nambiar, M.K., Nahian, M.R., Bueno, B., Mackey, C., Vasanthakumar, S., Nazarian, N., Krayenhoff, E.S., Norford, L.K. and Aliabadi, A.A. (2021) The vertical city weather generator (VCWG v1.3.2). *Geoscientific Model Development*, 14, 961–984 <https://gmd.copernicus.org/articles/14/961/2021/>.
- Nielsen-Gammon, J.W., McNider, R.T., Angevine, W.M., White, A.B. and Knupp, K. (2007) Mesoscale model performance with assimilation of wind profiler data: sensitivity to assimilation parameters and network configuration. *Journal of Geophysical Research: Atmospheres*, 112 <https://agupubs.onlinelibrary.wiley.com/doi/abs/10.1029/2006JD007633>.
- Otte, T.L., Lacer, A., Dupont, S. and Ching, J.K.S. (2004) Implementation of an urban canopy parameterization in a mesoscale meteorological model. *Journal of Applied Meteorology*, 43, 1648–1665 <https://journals.ametsoc.org/view/journals/apme/43/11/jam2164.1.xml>.
- Park, M.-S., Ho, C.-H., Kim, J. and Elsberry, R.L. (2011) Diurnal circulations and their multi-scale interaction leading to rainfall over the South China Sea upstream of the Philippines during intraseasonal monsoon westerly wind bursts. *Climate Dynamics*, 37, 1483–1499. <https://doi.org/10.1007/s00382-010-0922-z>.
- Peings, Y., Saint-Martin, D. and Douville, H. (2012) A numerical sensitivity study of the influence of Siberian snow on the northern annular mode. *Journal of Climate*, 25, 592–607 <https://journals.ametsoc.org/view/journals/clim/25/2/jcli-d-11-00038.1.xml>.

- Raupach, M.R., Antonia, R.A. and Rajagopalan, S. (1991) Rough-Wall turbulent boundary layers. *Applied Mechanics Reviews*, 44, 1–25. <https://doi.org/10.1115/1.3119492>.
- Ries, H., Schlünzen, K.H., Brümmner, B., Claussen, M. and Müller, G. (2010) Impact of surface parameter uncertainties on the development of a trough in the Fram Strait region. *Tellus A*, 62, 377–392 <https://onlinelibrary.wiley.com/doi/abs/10.1111/j.1600-0870.2%010.00451.x>.
- Rotach, M.W., Vogt, R., Bernhofer, C., Batchvarova, E., Christen, A., Clappier, A., Feddersen, B., Gryning, S.-E., Martucci, G., Mayer, H., Mitev, V., Oke, T.R., Parlow, E., Richner, H., Roth, M., Roulet, Y.-A., Ruffieux, D., Salmond, J.A., Schatzmann, M. and Voogt, J.A. (2005) BUBBLE—an urban boundary layer meteorology project. *Theoretical and Applied Climatology*, 81, 231–261. <https://doi.org/10.1007/s00704-004-0117-9>.
- Roth, M. (2000) Review of atmospheric turbulence over cities. *Quarterly Journal of the Royal Meteorological Society*, 126, 941–990. <https://doi.org/10.1256/smsqj.56408>.
- Salim, M.H., Schlünzen, K.H. and Grawe, D. (2015) Including trees in the numerical simulations of the wind flow in urban areas: should we care? *Journal of Wind Engineering and Industrial Aerodynamics*, 144, 84–95 <https://www.sciencedirect.com/science/article/pii/S0167610515001178>.
- Salim, M.H., Schlünzen, K.H., Grawe, D., Böttcher, M., Gierisch, A.M.U. and Fock, B.H. (2018) The microscale obstacle-resolving meteorological model MITRAS v2.0: model theory. *Geoscientific Model Development*, 11, 3427–3445 <https://gmd.copernicus.org/articles/11/3427/2018/>.
- Schlünzen, K.H. (1990) Numerical studies on the inland penetration of sea breeze fronts at a coastline with tidally flooded mudflats. *Contributions to Atmospheric Physics*, 63, 243–256.
- Schlünzen, K.H., Böttcher, M., Fock, B.H., Gierisch, A., Grawe, D. and Salim, M. (2018) Scientific documentation of the multiscale model system M-SYS. (METRAS, MITRAS, MECTM, MICTM, MESIM). MEMI Technical Report 4 <https://www.mi.uni-hamburg.de/en/arbeitsgruppen/memi/modelle/dokumentation/msys-scientific-documentation-20180706.pdf>.
- Schlünzen, K.H., Grawe, D., Bohnenstengel, S.I., Schlüter, I. and Koppmann, R. (2011) Joint modelling of obstacle induced and mesoscale changes—current limits and challenges. *Journal of Wind Engineering and Industrial Aerodynamics*, 99, 217–225 <https://www.sciencedirect.com/science/article/pii/S0167610511000110>.
- Schlünzen, K.H., Hinneburg, D., Knoth, O., Lambrecht, M., Leitl, B., Lopez, S., Lüpkes, C., Pankus, H., Renner, E., Schatzmann, M., Schoenmeyer, T., Trepte, S. and Wolke, R. (2003) Flow and transport in the obstacle layer: first results of the micro-scale model MITRAS. *Journal of Atmospheric Chemistry*, 44, 113–130. <https://doi.org/10.1023/A:1022420130032>.
- Schlünzen, K.H., Hoffmann, P., Rosenhagen, G. and Riecke, W. (2010) Long-term changes and regional differences in temperature and precipitation in the metropolitan area of Hamburg. *International Journal of Climatology*, 30, 1121–1136 <https://rmets.onlinelibrary.wiley.com/doi/abs/10.1002/joc.1968>.
- Schlünzen, K.H. and Katzfey, J.J. (2003) Relevance of sub-grid-scale land-use effects for mesoscale models. *Tellus A: Dynamic Meteorology and Oceanography*, 55, 232–246. <https://doi.org/10.3402/tellusa.v55i3.12095>.
- Schraff, C., Reich, H., Rhodin, A., Schomburg, A., Stephan, K., Perriñez, A. and Potthast, R. (2016) Kilometre-scale ensemble data assimilation for the COSMO model (KENDA). *Quarterly Journal of the Royal Meteorological Society*, 142, 1453–1472 <https://rmets.onlinelibrary.wiley.com/doi/abs/10.1002/qj.2748>.
- Schraff, C.H. (1997) Mesoscale data assimilation and prediction of low stratus in the alpine region. *Meteorology and Atmospheric Physics*, 64, 21–50. <https://doi.org/10.1007/BF01044128>.
- Skamarock, W.C., Klemp, J.B., Dudhia, J., Gill, D.O., Liu, Z., Berner, J., Wang, W., Powers, J.G., Duda, M.G., Barker, D.M. and Huang, X.-Y. (2019) A Description of the Advanced Research WRF Version 4. (No. NCAR/TN-556+STR). <https://doi.org/10.5065/1dfh-6p97>.
- Solman, S.A. and Pessacg, N.L. (2012) Regional climate simulations over South America: sensitivity to model physics and to the treatment of lateral boundary conditions using the MM5 model. *Climate Dynamics*, 38, 281–300. <https://doi.org/10.1007/s00382-011-1049-6>.
- Srinivas, C.V., Yesubabu, V., Venkatesan, R. and Ramarkrishna, S.S.V.S. (2010) Impact of assimilation of conventional and satellite meteorological observations on the numerical simulation of a bay of Bengal tropical cyclone of November 2008 near Tamil Nadu using WRF model. *Meteorology and Atmospheric Physics*, 110, 19–44. <https://doi.org/10.1007/s00703-010-0102-z>.
- Stauffer, D.R., Seaman, N.L. and Binkowski, F.S. (1991) Use of four-dimensional data assimilation in a limited-area mesoscale model part II: effects of data assimilation within the planetary boundary layer. *Monthly Weather Review*, 119, 734–754 [https://journals.ametsoc.org/view/journals/mwre/119/3/1520-0493\\_1991\\_119\\_0734\\_uofdda\\_2\\_0\\_co\\_2.xml](https://journals.ametsoc.org/view/journals/mwre/119/3/1520-0493_1991_119_0734_uofdda_2_0_co_2.xml).
- Stensrud, D.J. and Bao, J.-W. (1992) Behaviors of variational and nudging assimilation techniques with a chaotic low-order model. *Monthly Weather Review*, 120, 3016–3028 [https://journals.ametsoc.org/view/journals/mwre/120/12/1520-0493\\_1992\\_120\\_3016\\_bovana\\_2\\_0\\_co\\_2.xml](https://journals.ametsoc.org/view/journals/mwre/120/12/1520-0493_1992_120_3016_bovana_2_0_co_2.xml).
- Stewart, I.D. and Oke, T.R. (2012) Local climate zones for urban temperature studies. *Bulletin of the American Meteorological Society*, 93, 1879–1900.
- von Salzen, K., Claussen, M.M. and Schlünzen, K.H. (1996) Application of the concept of blending height to the calculation of surface fluxes in a mesoscale model. *Meteorologische Zeitschrift*, 5, 60–66. <https://doi.org/10.1127/metz/5/1996/60>.
- Voss, V. (2023) High resolution obstacle-resolved model results for the city centre of Hamburg, Germany, from the microscale transport and stream model MITRAS on 21 June 2000. [https://www.wdc-climate.de/ui/entry?acronym=MITRAS\\_ATMODAT](https://www.wdc-climate.de/ui/entry?acronym=MITRAS_ATMODAT).
- Wang, H., Liu, Y., Zhao, T., Liu, Y., Xu, M., Shen, S., Jiang, Y., Yang, H. and Feng, S. (2018) Continuous assimilation of lightning data using time-lagged ensembles for a convection-allowing numerical weather prediction model. *Journal of Geophysical Research: Atmospheres*, 123, 9652–9673 <https://agupubs.onlinelibrary.wiley.com/doi/abs/10.1029/2018JD028494>.
- WMO. (2023) In: Schlünzen, K.H., Grimmond, S. and Baklanov, A. (Eds.) *Guidance on Measuring, Modelling and Monitoring the Canopy Layer Urban Heat Island (CL-UHI)*. Geneva, Switzerland: World Meteorological Organization, WMO-No. 1292.
- Zängl, G., Reinert, D. and Prill, F. (2022) Grid refinement in ICON v2.6.4. *Geoscientific Model Development*, 15, 7153–7176. <https://doi.org/10.5194/gmd-15-7153-2022>.



Zou, X., Navon, I.M. and Ledimet, F.X. (1992) An optimal nudging data assimilation scheme using parameter estimation. *Quarterly Journal of the Royal Meteorological Society*, 118, 1163–1186 <https://rmets.onlinelibrary.wiley.com/doi/abs/10.1002/qj.49711850808>.

### SUPPORTING INFORMATION

Additional supporting information can be found online in the Supporting Information section at the end of this article.

**How to cite this article:** Cheng, G., Schlünzen, K.H., Grawe, D., Voss, V., Thatcher, M. & Rayner, P. (2023) Parameterizing building effects on airflows within the urban canopy layer for high-resolution models using a nudging approach. *Quarterly Journal of the Royal Meteorological Society*, 149(755), 2617–2633. Available from: <https://doi.org/10.1002/qj.4524>